Crystallization behavior and magnetic properties of Cu-containing Fe–Cr–Mo–Ga–P–C–B alloys

J. M. Borrego, C. F. Conde, and A. Conde[a)]
*Departamento de Física de la Materia Condensada, Instituto de Ciencia de Materiales, CSIC.,
Universidad de Sevilla, P.O. Box 1065, 41080 Sevilla, Spain*

M. Stoica[b)] and S. Roth
IFW Dresden, Institut für Metallische Werkstoffe, Postfach 270016, D-01171 Dresden, Germany

J. M. Greneche
*Laboratoire de Physique de l'Etat Condensé, UMR CNRS 6087, Université du Maine,
F-72085 Le Mans Cedex 9, France*

Multicomponent $Fe_{65.5}Cr_4Mo_4Ga_4P_{12}C_5B_{5.5}$ amorphous alloy is known to have good soft magnetic properties combined with large glass-forming ability. Searching for a nanocrystalline structure that could improve its magnetic properties, Cr and Mo were partially substituted by Cu. The devitrification process of Cu-containing alloys shows an additional broad crystallization event that can be described by an Avrami law, with an exponent close to unity, typical for nanocrystallization phenomena. The microstructure of the nanocrystalline alloys consists of Fe(Ga) nanocrystals with a mean grain size of $5-10$ nm embedded in an amorphous matrix. The maximum crystalline volume fraction achieved at the end of the nanocrystallization process was found to be of around 20% and for alloys with high Cu content a number of crystals of larger size (~40 nm) were observed. The combined use of x-ray diffraction and Mössbauer spectrometry allowed to estimate the compositions of both the nanocrystalline grains and the amorphous residual phase of nanocrystalline alloys. The complex hyperfine structure of the studied alloys at the end of the nanocrystallization process was characterized. © *2006 American Institute of Physics*. [DOI: 10.1063/1.2234536]

I. INTRODUCTION

Bulk nanocrystalline materials with controllable microstructure and properties are expected to have excellent application potentiality. Their wide supercooled liquid region and high thermal stability against crystallization allow a broad time and temperature range to control the nucleation and growth of nanocrystals.[1] Recently minor alloying addition or microalloying technology is found to have significant effect on the glass-forming ability, the microstructure, and the magnetic properties of bulk metallic glasses.[2–4]

$Fe_{65.5}Cr_4Mo_4Ga_4P_{12}C_5B_{5.5}$ amorphous alloy is known to have a large glass-forming ability that makes possible its production in bulk form. Amorphous rods up to 4 mm in diameter and disks with 10 mm diameter and 1 mm thickness were obtained by flux-melting and water quenching techniques and copper mold casting.[5,6] This large glass-forming ability combined with good soft magnetic properties[6] results in a very promising material.

The aim of this study was to obtain a nanocrystalline alloy based on that composition that would combine the high glass-forming ability of the base alloy and the excellent magnetic properties of the nanocrystalline microstructure. The effects of the Cr and Mo substitution by Cu on the crystallization behavior and magnetic properties of FeCr-

MoCuGaPCB alloys (Table I) have been investigated by differential scanning calorimetry (DSC), thermomagnetic gravimetry, x-ray diffractometry (XRD), Mössbauer spectrometry, transmission electron microscopy (TEM), and magnetic measurements.

Due to the structural complexity of the nanocrystalline alloys and, in particular, of their hyperfine structure, previous results obtained for arc-melted polycrystalline FeGa binary alloys[7] were used in the characterization of structural and hyperfine parameters of FeGa crystalline grains.

II. EXPERIMENT

Multicomponent $Fe_{65.5}Cr_{4-x}Mo_{4-y}Cu_{x+y}Ga_4P_{12}C_5B_{5.5}$ $(x,y=0,0.5,1)$ master alloy ingots were obtained by induction melting starting from Fe–B, Fe–C, and Fe–P prealloys and Mo (99.4% purity), Cr (99.99% purity), Fe (99.9% purity), and crystalline B (99.99% purity). From these alloys, 10 mm wide and 25 μm thick amorphous ribbons were prepared by a single-roller melt-spinning technique. Amorphous alloys are labeled A, B, C, D, E, and F and their compositions are given in Table I. Nanocrystalline alloys were obtained after a subsequent annealing under argon atmosphere at temperatures determined from calorimetric measurements.

X-ray diffraction patterns were recorded at room temperature using a Brücker AXS D8-Advance diffractometer with Cu $K\alpha$ radiation. Electron microscopy observations were performed using an electron microscope Philips CM200 operated at 200 kV.

[a)]Electronic mail: conde@us.es
[b)]Present address: LTPCM-CNRS UA29, ENSEEG, Institut National Politechnique de Grenoble, Domain Universitaire, 1136 Rue de la Piscine, BP 75 St. Martin d'Hères Campus 38402, France.

     100, 043515-1

TABLE I. Glass transition onset T_g and crystallization onset T_x temperatures, at 20 K/min. Activation energy and Avrami exponent of the first crystallization stage, $E_{a,1}$ and n_1, respectively, and activation energy of the second crystallization stage, $E_{a,2}$, for $Fe_{65.5}Cr_{4-x}Mo_{4-y}Cu_{x+y}Ga_4P_{12}C_5B_{5.5}$ alloys.

Alloy	x	y	T_g (K) ±5	T_x (K) ±1	$E_{a,1}$ (eV) ±0.2	n_1 ±0.2	$E_{a,2}$ (eV) ±0.2
A	0	0	736	798	⋯	⋯	3.4
B	0.5	0	702	750	3.5	1.3	5.6
C	0	0.5	702	750	3.5	1.3	5.6
D	1	0	⋯	754	3.9	1.2	5.4
E	0	1	⋯	754	3.9	1.2	5.5
F	1	1	⋯	757	4.0	1.3	5.7

The values of the glass transition onset T_g, the crystallization onset T_x, and the crystallization peak T_p temperatures were determined by differential scanning calorimetry. The experiments were performed with a Perkin-Elmer DSC-7 under a continuous argon flow. The glass transition onset was defined as the point of intersection between the linearly extrapolated curve below the transition with the steepest tangent of the rise in the heat flow signal.[8] The melting behavior was studied with a Netzsch 404 DSC calorimeter at a heating rate of 20 K/min. The liquidus temperature T_l was determined as the inflection point of the last endotherm of the heating curve (high temperature side).

For thermomagnetic experiments the magnetic field of a small magnet (~15 mT) was applied to the sample and the temperature variation of the magnetic force was recorded as an apparent weight change of the sample (Perkin-Elmer TGA-7). The Curie temperature T_C was determined from $M(T)$ curves, fitting the data near T_C to a critical law of the form $M(T) \propto (T-T_C)^\beta$ with $\beta=0.36$, and extrapolating to $M=0$.

The saturation magnetization M_s at room temperature was measured with a Lakeshore 7407 vibrating sample magnetometer, using a maximum applied field of 15 kOe. The coercive field H_c was measured at room temperature with a Förster Koerzimat.

Mössbauer spectra were taken at 300 K in a transmission geometry using a ^{57}Co(Rh) source, with the γ beam perpendicular to the ribbon plane. The values of hyperfine parameters were refined using NORMOS program.[9] The isomer shift values are quoted relative to α-Fe at 300 K.

III. RESULTS AND DISCUSSION

A. As-quenched alloys

The amorphous character of as-quenched Cu-free and 0.5 at. % Cu-containing alloys was confirmed by transmission electron microscopy. TEM images of these alloys [Fig. 1(a)] only show the homogeneous hazy contrast, which is known to be characteristic of an amorphous structure and the diffraction patterns have only diffuse haloes. As-quenched samples with higher Cu content show a nanocrystalline microstructure consisting of a small density of bcc-Fe grains (5–10 nm for 1 at. % Cu and 20–30 nm for 2 at. % Cu) randomly dispersed in an amorphous matrix with a crystalline volume fraction lower than 5% [Figs. 1(b) and 1(c)]. However, in selected area diffraction patterns, crystalline spots due to the emerging bcc-Fe phase are only visible for the alloy with 2 at. % Cu [Fig. 1(c)].

Mössbauer spectra at 300 K of as-quenched alloys (Fig. 2) show the six-line pattern characteristic of amorphous ferromagnetic alloys, moderately collapsed due to the proximity

FIG. 2. (Color online) Transmission Mössbauer spectra, at 300 K, and their corresponding fitting (solid line) and magnetic hyperfine field distributions (right) of as-quenched alloys B (0.5 at. % Cu), D (1 at. % Cu), and F (2 at. % Cu).
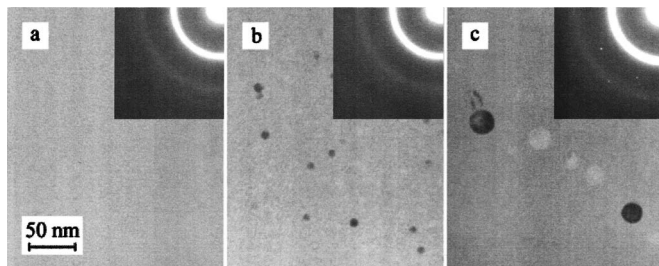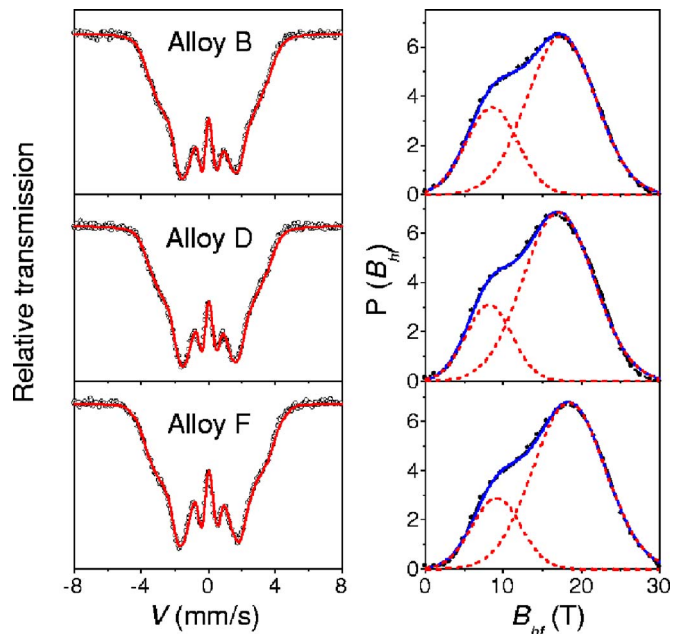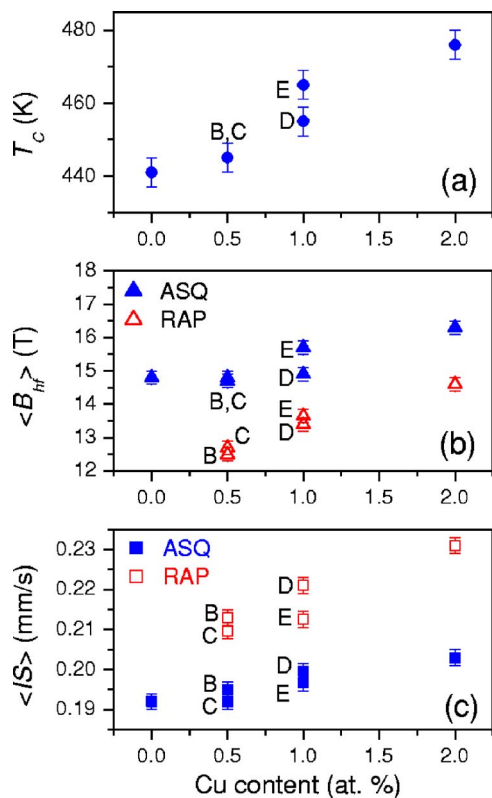
FIG. 1. Transmission electron microscopy images and diffraction patterns of as-quenched alloys: (a) B (0.5 at. % Cu), (b) D (1 at. % Cu), and (c) F (2 at. % Cu).

FIG. 3. (Color online) Compositional dependence of (a) Curie temperature T_C of the as-quenched alloys. [(b) and (c)] average magnetic hyperfine field $\langle B_{hf} \rangle$ and average isomer shift $\langle IS \rangle$ of as-quenched (ASQ) alloys and residual amorphous (RA) phase of nanocrystalline alloys, respectively.
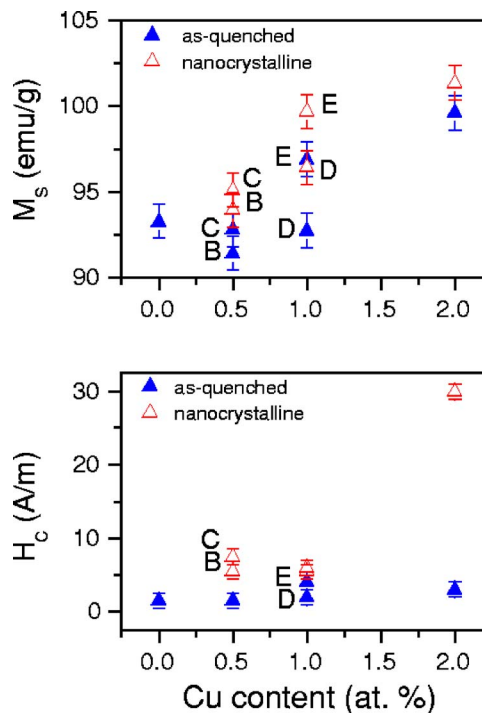

FIG. 4. (Color online) Saturation magnetization M_S at 300 K (above) and coercive field H_c (below) of as-quenched and nanocrystalline alloys as a function of the Cu content.

of the Curie temperature of these alloys to room temperature. The presence of bcc-Fe crystals is not evidenced in MS, even for alloys with Cu content ≥ 1 at. %, due to their low volume fraction. The data were fitted using a discrete magnetic hyperfine field distribution (HFD), with the quadrupolar shift averaged to zero. In order to reproduce the asymmetrical shape of the spectra, a linear correlation between the magnetic hyperfine field and the isomer shift of the components of the distribution was introduced.[10]

For all alloys, HFDs can be approximately described by two Gaussian components. Such behavior can be attributed to the presence of two main kinds of iron environments in the amorphous as-cast state. The peak position of the high field (HF) component (Fig. 2) displays a weak tendency to shift to higher field values with decreasing Cr and Mo contents that, as it will be shown below, becomes more pronounced in the case of nanocrystalline alloys. This occurrence seems to indicate that the HF component can be ascribed to sites where Fe atoms are preferentially surrounded by Fe, Ga(P), and B(C) atoms,[7,11] and also by Cr(Mo). The low field (LF) component can be attributed to Fe atoms preferentially surrounded by B(C) and Cu atoms.[11]

The Curie temperature T_C and the average magnetic hyperfine field $\langle B_{hf} \rangle$, at 300 K, of the as-quenched alloys are enhanced with Cr and Mo replacement [Figs. 3(a) and 3(b), respectively]. The effect of the lowering of the Curie temperature with Cr and Mo addition (of ~ 20 K/at. %) is similar to that previously found in Fe(Cr)SiBCuNb (Ref. 12) and Fe(Mo)SiBCuNb (Ref. 13) amorphous alloys. The average

isomer shift $\langle IS \rangle$ also increases with the substitution of Cr and Mo by Cu, being the increment more noticeable in the case of Cr replacement [Fig. 3(c)]. In addition, the presence of an in-plane texture of magnetic domains can be concluded for all the alloys. This preferential orientation is consistent with the presence of large quenched-in stresses.

Figure 4 shows the saturation magnetization M_s at 300 K (above) and coercive field H_c (below) of as-quenched samples as a function of the Cu content. The saturation magnetization follows the same tendency as T_C and $\langle B_{hf} \rangle$, with values ranging from 90 to 100 emu/g. The coercive field, lower than 4 A/m, is not altered with Cu substitution.

B. Crystallization and melting behavior

Figure 5 shows the DSC curves, at 20 K/min, of as-quenched alloys. The curves corresponding to Cu-free and 0.5 at. % Cu-containing alloys exhibit the endothermic event characteristic of the glass transition, followed by a supercooled liquid region (SLR). The remarkable width of this region, $\Delta T_x = T_g - T_x$, ranging from 62 to 48 K with increasing Cu content (Table I), is indicative of the high thermal stability of the supercooled liquid. The SLR is absent in the alloys with higher Cu content.

The melting curves of all the alloys at a heating rate of 20 K/min are shown in Fig. 6. The curves corresponding to Cu-free and 0.5 and 1 at. % Cu-containing alloys exhibit a melting behavior very near to a eutectic point while the curves corresponding to the alloy with 2 at. % Cu displays two clear melting peaks indicating that it is off eutectic. The calculated values of T_g / T_l, ranging from 0.57 (for 0 at. %
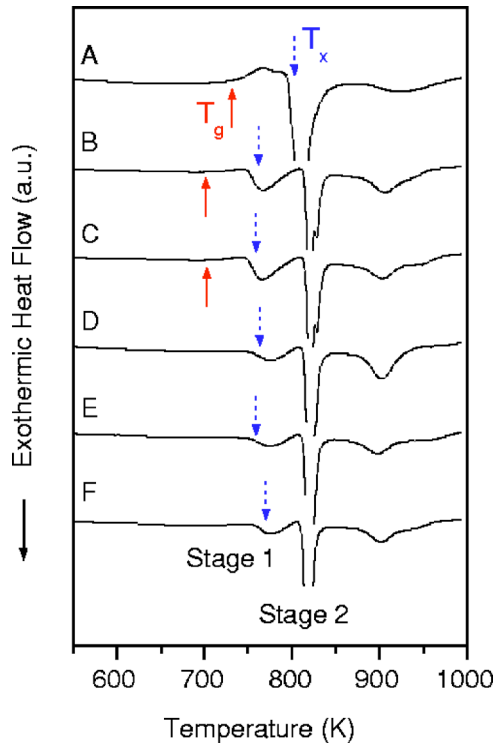
FIG. 5. (Color online) DSC curves, at 20 K/min, of as-quenched alloys.

FIG. 6. Melting curves, at 20 K/min, of as-quenched alloys.

Cu) to 0.54 (for 0.5 at. % Cu) (Table I), are lower than but close to 2/3,[14] reflecting the good glass-forming ability of the present alloys.

The devitrification process of the Cu-free alloy consists of two main stages revealed by two well separated exothermic peaks. When Cu is added to the alloy an additional DSC exotherm appears at lower temperatures (Fig. 5). This additional broad crystallization peak is typical for nanocrystallization processes. The apparent activation energy values of the nanocrystallization stage, $E_{a,1}$, evaluated by the Kissinger method,[15] range from 3.5 to 4.0 eV (Table I), increasing with the Cu content of the alloy in the same order as the crystallization onset temperature. The Avrami exponent was estimated by the maximum reaction rate equation derived by Gao *et al.*[16] and the obtained low value $\sim$1.3 is also typical for nanocrystalline alloys.

XRD patterns confirm that the microstructure of Cu-containing samples heated up to the first DSC exotherm consists of bcc-Fe nanocrystalline grains embedded in an amorphous matrix in all cases. As an example, Fig. 7 shows the scan corresponding to alloy D heated up to the end of the nanocrystallization process.

XRD scans, shown in Fig. 7, reveal the different crystallized phases formed in this crystallization process: α-Fe and Fe_3C in the case of Cu-containing alloys and an additional phase, $Fe_{23}(C,B)_6$, in the case of Cu-free alloy.

C. Nanocrystalline alloys

In order to study the microstructural characteristics and the magnetic properties of the nanocrystalline alloys, Cu-containing amorphous ribbons were heated up to the end of the first DSC exotherm. The compositions of both the nano-
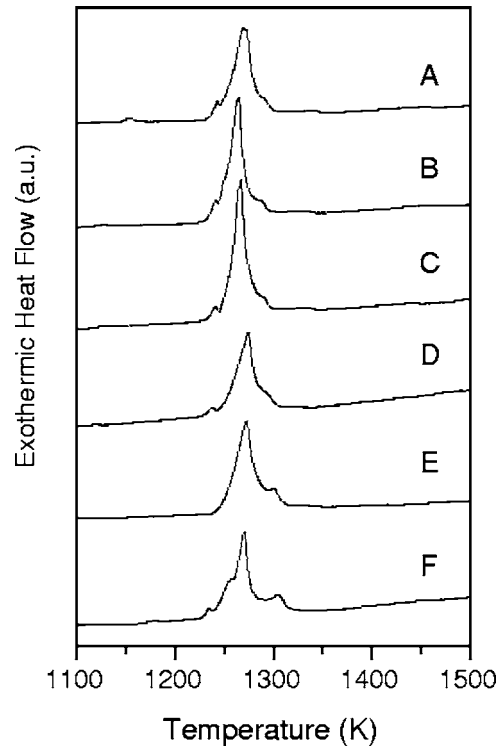
crystalline grains and the amorphous residual phase and the maximum crystalline fraction attainable in the nanocrystallization process were determined by combining Mössbauer spectrometry and x-ray diffraction.

The composition of the nanocrystalline grains was first calculated from XRD analysis. The lattice parameter of the nanocrystalline phase, $a = 2.900(5)$ Å, was found to be larger than the lattice parameter for pure bcc Fe (2.866 Å), suggesting that the crystalline grains might contain some Ga in a solid solution of Fe(Ga). Due to the low solubility of Cr, Mo, and B atoms in the Fe lattice, the Ga concentration in the Fe(Ga) phase of the annealed samples can be estimated from the relationship between the lattice parameter in FeGa binary alloys and the Ga content, z,[7]

$$a \text{ (Å)} = 2.869(2) + 0.0020(1)z, \tag{1}$$

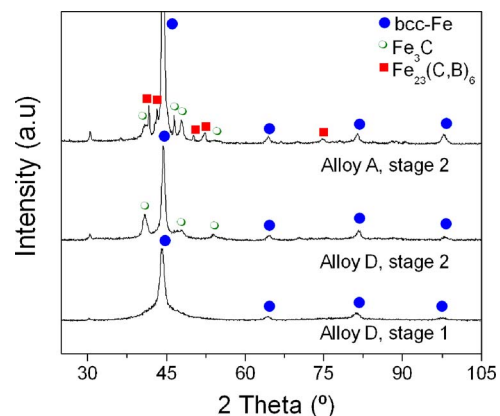and a value in the range of $14(2)-16(2)$ at. % Ga was found.

FIG. 7. (Color online) X-ray diffraction patterns corresponding to samples of alloy D heated up to the end of the first DSC exotherm and samples of alloys A and D heated up to the end of the second DSC exotherm.
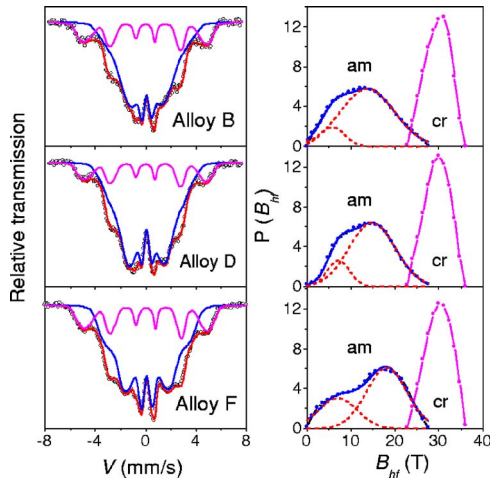
FIG. 8. (Color online) Transmission Mössbauer spectra at 300 K and their fitting of nanocrystalline alloys B (0.5 at. % Cu), D (1 at. % Cu), and F (2 at. % Cu). Their corresponding magnetic hyperfine field distributions are shown on the right.

An analysis of the intensity profile of the main diffraction maximum was used to determine the amount of the crystalline fraction induced by the thermal treatment. Both the amorphous halo and the (110) diffraction line of the bcc-Fe(Ga) phase were fitted, after background subtraction by using pseudo-Voigt functions.[17] Due to the difference between the average scattering power of these two phases, a weighting factor should be used for the respective integrated intensities.[18] An average scattering power for phase i of the form $\langle f \rangle_i = \Sigma_\beta C_{\beta,i} f_\beta$ was defined, where $C_{\beta,i}$ is the concentration of the β element of scattering factor f_β in the i phase (amorphous or crystalline). Assuming that the total integrated intensity of the amorphous halo plus that of the (110) bcc-Fe(Ga) peak is a constant, it can be written as

$$\langle f \rangle_{IA}^2 = x_c \langle f \rangle_{NC}^2 + (1 - x_c) \langle f \rangle_{RA}^2, \tag{2}$$

where IA denotes "initial amorphous," NC denotes "nanocrystalline," and RA denotes "residual amorphous" phases. Therefore, the crystalline volume fraction x_c can be obtained from

$$\frac{A_{NC}}{A_{NC} + A_{RA}} = \frac{x_c \langle f \rangle_{NC}^2}{x_c \langle f \rangle_{NC}^2 + (1 - x_c) \langle f \rangle_{RA}^2}, \tag{3}$$

where A_i is the integrated intensity of the deconvoluted profile corresponding to the i phase. The crystalline volume fraction x_c achieved at the end of the nanocrystallization process was found to be around 20(5)%.

Mössbauer spectra of nanocrystalline alloys at 300 K (Fig. 8) show the emergence of additional broad exterior lines originating from the Fe(Ga) nanocrystals, superimposed with the broad collapsed sextet attributed to the residual amorphous phase. In a previous study,[7] Mössbauer spectra of FeGa crystalline binary alloys, at 300 K, were best fitted using a discrete hyperfine magnetic field distribution with a linear correlation between the magnetic hyperfine field and the isomer shift of the components of the distribution and the quadrupolar shift averaged to zero. It was found that the Ga content of the binary alloy determines the limits of the HFD,

the average magnetic hyperfine field, and the average isomer shift of the distribution. $\langle B_{hf} \rangle$ shows a decrease with Ga content, z, that can be expressed by a linear relation for z up to 20 at. % Ga,[7]

$$\langle B_{hf} \rangle \ (T) = 33.1(3) - 0.23(2)z, \tag{4}$$

and the average isomer shift $\langle IS \rangle$ also increases linearly with Ga content up to 20 at. % Ga following the relation[7]

$$\langle IS \rangle \ (mm/s) = -0.003(5) + 0.0070(5)z. \tag{5}$$

Taking into account the previous results, Mössbauer spectra of the nanocrystalline alloys were fittted using two magnetic hyperfine field distributions associated with the Fe(Ga) nanocrystalline phase and to the residual amorphous phase, respectively. In both of them the quadrupolar shift was averaged to zero and in order to reproduce the asymmetrical shape of the spectra, a linear correlation between the magnetic hyperfine field and the isomer shift of the components of the distributions was introduced. As an example, Fig. 8 shows the magnetic hyperfine field distributions of these nanocrystalline alloys with different Cu contents.

HFDs of the residual amorphous phase also show the "double peak" structure found in the as-quenched alloy. The peak position of the low field component ($\sim$6.5 T) was found to be almost independent of the Cr and Mo contents, while the high field component shifts from 13.5 to 18 T with decreasing Cr and Mo concentrations. This result corroborates the ascription of the high field component to Fe atoms preferentially surrounded by Fe, P(Ga), and B(C),[7,11] and also by Cr and Mo atoms, that was suggested for as-quenched alloys. Values of $\langle B_{hf} \rangle$, shown in Fig. 3(b), lower than those of the initial amorphous phase due to the depletion in Fe are significantly enhanced with Cr and Mo replacement. The $\langle IS \rangle$ values, shown in Fig. 3(c), increase in the same alloy sequence as those of the initial amorphous alloy.

No significant differences in the magnetic hyperfine field distribution of the crystalline phase of the different alloys were found, with an average magnetic hyperfine field of about 29.7(3) T and an average isomer shift of 0.113(3) mm/s. These values correspond, according to Eqs. (4) and (5), to 15(2) and 17(2) at. % Ga content, respectively, in accordance with XRD results.

The atomic fraction of Fe atoms in the crystalline phase, estimated from the relative crystalline-amorphous absorption areas (assuming the same values of f-recoil-less factors for both phases), was found to be about 20% in all cases. As the composition of the nanocrystals is estimated at $Fe_{84}Ga_{16}$, the approximate composition of the residual amorphous matrix results to $Fe_{62}Cr_{4.5}Mo_{4.5}Cu_{0.5}Ga_2P_{14}C_6B_{6.5}$.

TEM images reveal that the microstructure of the nanocrystalline samples does depend only on the Cu content regardless the refractory substitution (Cr or Mo). Electron microscopy images of nanocrystalline samples of 0.5 and 1 at. % Cu-containing alloys [Figs. 9(a) and 9(b), respectively] show the presence of bcc-Fe(Ga) crystals, with a mean grain size of 5–10 nm for 0.5 at. % Cu and 10–20 nm for 1 at. % Cu, randomly dispersed in an amorphous matrix. The microstructure of 2 at. % Cu-alloy sample heated up to
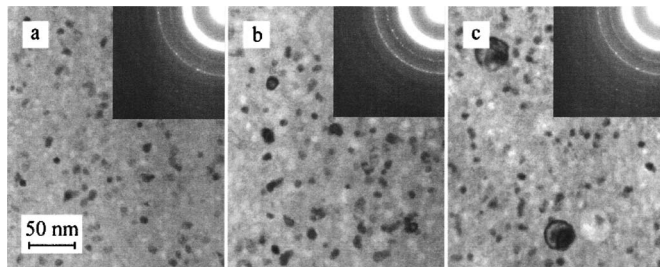
FIG. 9. Transmission electron microscopy images and diffraction patterns of nanocrystalline alloys (a) B (0.5 at. % Cu), (b) D (1 at. % Cu), and (c) F (2 at. % Cu).

the first crystallization peak show two types of bcc-Fe(Ga) grains [Fig. 9(c)]: crystals with a mean diameter of 40 nm, grown from the quenched-in nuclei, and crystals with a mean size of 5–10 nm that emerge from the initial amorphous. The identification of the nanocrystals was confirmed from electron diffraction patterns (Fig. 9) that only show the rings of bcc phase.

The saturation magnetization of the nanocrystalline samples increases only up to 5% with respect to the value corresponding to the as-quenched alloys (Fig. 4). This result contrasts with the remarkable increment of the saturation magnetization, from 0.9 to 1.4 T, after the nanocrystallization of $Fe_{74}Al_4Ga_2P_{11}B_4Si_4Cu_1$ amorphous alloy.[19] The coercive field slightly increases up to 6 A/m for 0.5 and 1 at. % Cu-containing alloys but a significant magnetic hardening is observed for the 2 at. % Cu-containing alloy, with a coercive field of 30 A/m (Fig. 4).

IV. CONCLUSIONS

Appropriate thermal treatment of Cu-containing $Fe_{65.5}Cr_{4-x}Mo_{4-y}Cu_{x+y}Ga_4P_{12}C_5B_{5.5}$ alloys leads to a nanocrystalline microstructure consisting of Fe(Ga) nanocrystals embedded in a residual amorphous matrix. The Curie temperature, the magnetic hyperfine field, and the saturation magnetization of the as-quenched samples are enhanced with Cr and Mo replacement while the coercive field, lower than 4 A/m, is not altered with Cu substitution.

However, the substitution of Cr and Mo by Cu decreases the glass-forming ability of the initial alloy and the maximum crystalline volume fraction achieved at the end of the nanocrystallization process was found to be only around 20%.

By combining Mössbauer spectrometry and x-ray diffraction analysis, the compositions of both the nanocrystalline grains and the amorphous residual phase of nanocrystalline alloys were modelled. The complex hyperfine structure of the studied alloys at the end of the nanocrystallization process was characterized.

[1] W. L. Johnson, MRS Bull. **24**, 42 (1999).
[2] W. H. Wang, M. X. Pan, D. Q. Zhao, Y. Hu, and H. Y. Bai, J. Phys.: Condens. Matter **16**, 3719 (2004).
[3] Z. Zhang, D. Q. Zhao, and W. H. Wang, J. Mater. Res. **20**, 314 (2005).
[4] Y. T. Wang, Z. Y. Pang, R. J. Wang, D. Q. Zhao, M. X. Pan, B. S. Han, W. L. Wang, and W. H. Wang, J. Non-Cryst. Solids **352**, 444 (2006).
[5] T. D. Shen and R. B. Schwarz, Appl. Phys. Lett. **75**, 49 (1999).
[6] M. Stoica, S. Roth, J. Eckert, L. Shultz, and M. D. Baró, J. Magn. Magn. Mater. **290–291**, 1480 (2005).
[7] J. M. Borrego, J. S. Blázquez, C. F. Conde, A. Conde, and S. Roth, Intermetallics (unpublished).
[8] R. Brüning and K. Samwer, Phys. Rev. B **46**, 11318 (1992).
[9] R. A. Brand, J. Lauer, and D. M. Herlach, J. Phys. F: Met. Phys. **12**, 675 (1983).
[10] I. Vincze, Solid State Commun. **25**, 689 (1978).
[11] M. Miglierini, J. Phys.: Condens. Matter **6**, 1431 (1994).
[12] C. F. Conde, M. Millán, and A. Conde, J. Magn. Magn. Mater. **138**, 314 (1994).
[13] C. F. Conde, V. Franco, and A. Conde, Philos. Mag. B **76**, 489 (1997).
[14] D. Turnbull, Contemp. Phys. **10**, 473 (1996).
[15] H. E. Kissinger, J. Res. Natl. Bur. Stand. **57**, 217 (1956).
[16] Y. Q. Gao, W. Wang, F. Q. Zheng, and X. Liu, J. Non-Cryst. Solids **81**, 135 (1986).
[17] A. Young and D. B. Wiles, J. Appl. Crystallogr. **15**, 430 (1982).
[18] J. S. Blázquez, V. Franco, C. F. Conde, and A. Conde, J. Magn. Magn. Mater. **254–255**, 460 (2003).
[19] K. Pekala, J. Latuch, T. Kulik, J. Antonowicz, and P. Jaskiewicz, Mater. Sci. Eng., A **375–377**, 377 (2004).